Diffraction imaging point of common-offset gather: GPR data example

J.J. S. de Figueiredo (DEP/UNICAMP, Brazil), F. Oliveira (CPGF/UFPA and FACEN/UFPA), E. Esmi (IMECC/UNICAMP, Brazil), L. Freitas (Geoprocessados, Mexico), S. Green (University of Houston, USA), A. Novais (IMECC/UNICAMP and INCT-GP, Brazil), and J. Schleicher (IMECC/UNICAMP and INCT-GP, Brazil)

Abstract

Hydrocarbon traps are generally located beneath complex geological structures. Such areas contain many seismic diffractors that carry detailed structure information in the order of the seismic wavelength. Therefore, the development of computational resources capable of detecting diffractor points with a good resolution is desirable, but has been a challenge in the area of seismic processing. In this work, we present a method for the detection of diffractor points in the common-offset gathers domain. In our approach, the diffraction imaging is based on the diffraction operator, which can be used in both the time and depth domains, in accordance with the complexity of the area. This method, which does not require any knowledge apart from the migration velocity field (i.e., rms velocities or interval velocities) applies pattern recognition to the amplitudes along the diffraction operator. Numerical examples using synthetic and real data demonstrate the feasibility of the technique.

Introduction

It is well known that hydrocarbon reservoirs commonly are located in geological stsructures that are difficult to image with seismic methods and obtain high resolution. This structures include common hydrocarbon traps, such as faults, pinch-outs, unconformities, salts domes, and other structures the size of which is of the order of the wavelength (Trorey, 1970).

Because of the importance of these types of structures, several methods for imaging diffractions have been developed in the recent past. The first authors to look into the topic were Landa et.al. (1987) and Landa and Keydar (1998), who proposed and refined a detection method related to specific kinematic and dynamic properties of diffracted waves. Another approach (Moser and Howard, 2008) is based on suppressing specular reflections to image diffractions in the depth domain. Most recently, Zhu and Wu (2010) developed a method based on the local image matrix (LIM), which uses an image condition in the local incident and reflection angles for source-receiver pairs to detect diffractions.

In this work, we propose a diffraction detection method based on an amplitude analysis along the elementary diffractions (Tabti et al., 2004). This method does not require any knowledge apart of from the migration velocity field, i.e., rms velocities or interval velocities depending on the complexity of the area. It applies pattern recognition to the amplitudes along the diffraction operator. Numerical examples on synthetic and ground penetrating radar (GPR) field data demonstrate the feasibility of the method.

Method

Diffraction operator

Tabti et al. (2004) introduced amplitude analysis along elementary diffractions for Fresnel aperture specification. As illustrated in Figure 1a, the traveltime of an elementary diffraction associated with a reflection point is tangent to the reflection traveltime at the stationary point (location of the specular reflection event). More specifically, in limited bandwidth situations, this tangential point becomes a tangential contact region, which defines the minimum aperture for true-amplitude Kirchhoff migration (Schleicher et. al., 1997). Tabti et al. (2004) named it the Fresnel aperture due to its close relationship to the Fresnel zone. For image point off any reflectors or diffractors, below referred to as “void image points”, there is no such region. The traveltime of the elementary diffraction associated with a void image point may cross some reflection events, but won’t be tangential to any events (see Figure 1b), except for extremely rare coincidental situations.

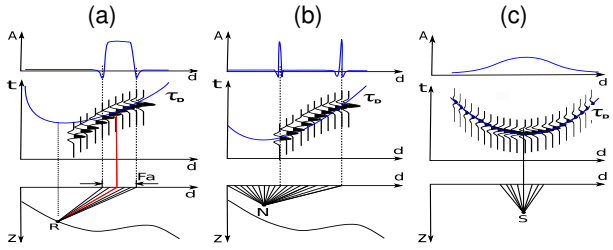

Figure 1: (Illustration of the diffraction operator for (a) a reflection point and (b) a void image point. Top: amplitude along the diffraction operator; center: diffraction traveltime and seismic event; bottom: image point and ray family. (c) Illustration of the diffraction operator for a diffraction point. Top: amplitude along the diffraction operator; center: diffraction traveltime and seismic event; bottom: image point and ray family.

Tabti et al. (2004) described amplitude analysis along elementary diffractions by means of a diffraction operator D. This operator derives from the Kirchhoff depth migration

integral (Schleicher et. al., 1993)

$$I(M) = \int_{A_f} d^2\xi \; W(M,\xi)\partial_t U(\xi,t)|_{t=\tau_D(M,\xi)} \qquad (1)$$

where $U(\xi,t)$ is the seismic data measured at ξ, $\tau_D(M,\xi)$ is the traveltime of the elementary diffraction of M, A_f is the Fresnel aperture, and $W(M,\xi)$ is a weight function. For simplicity, we omit the weight function in the present study, i.e. $W(M,\xi) = 1$. Integration variable ξ is the horizontal coordinate of the seismic section to be migrated, for instance the midpoint coordinate for a common-offset section or the receiver coordinate for a common-shot section.

Instead of performing the summation, the diffraction operator $D(M)$ at an image point M collects a single valued curve (or surface, in the 3D case), defined as a function of the integration variable ξ. Its value at ξ is the amplitude the stack in equation 1 will consider at ξ. This value defines the amplitude of the elementary diffraction measured at ξ. More specifically,

$$D(M,\xi) = W(M,\xi)\partial_t U(\xi,t)|_{t=\tau_D(M,\xi)} \; . \qquad (2)$$

In this paper, we restrict ourselves to a simplified version of the diffractor operator proposed by Tabti et al. (2004), based on the Kirchoff time migration integral for common-offset configuration. Therefore, the elementary diffraction traveltime $\tau_D(M,\xi)$ is given by (Landa et.al., 1987)

$$\tau_D(M,\xi) = \sqrt{(\frac{t_0}{2})^2 + (\frac{\xi - h}{2v})^2} + \sqrt{(\frac{t_0}{2})^2 + (\frac{\xi + h}{2v})^2} \qquad (3)$$

where t_0 is zero-offset time for any point at subsurface, h is the half-offset and v is medium velocity.

Tabti et al. (2004) also noted that in the case of a diffractor point (either a point scatterer or an edge), the corresponding elementary diffraction corresponds to the scattered seismic event. The Fresnel aperture then extends theoretically to infinity, regardless of the frequency content of the source pulse. Figure 1c illustrates the diffraction operator at a diffraction point.

Figures 1 form the basis of our diffraction imaging algorithm explained in the next section. The main idea of our detection method is to classify every point in the image domain M as a diffractor, reflector or void point by means of the characteristics of its diffraction operator $D(M,\xi)$. The approach consists in straightforward classification using a well-established pattern-recognition technique called k-nearest-neighbors (kNN).

Diffraction imaging by pattern recognition

Pattern recognition aims at classifying data (patterns) based either on a priori knowledge or on statistical information extracted from the patterns (Duda and Hart, 1973; Theodoridis and Koutroumbas, 1999). Pattern recognition techniques have found applications in various areas, for instance, decision making, inspection of objects, and automatic character recognition (Theodoridis and Koutroumbas, 1999).

The mathematical tool to achieve this aim is called a classifier. Suppose we are faced with the problem to classify a certain set of patterns into N classes, $w_1,\cdots,w_n$. Let $x_1,\cdots,x_p \in R^n$ be samples of patterns whose class is already known, and $C_i \subseteq \{x_1,\cdots,x_p\}$ be a subset of patterns associated with class w_i such that $C_j \cap C_i = \emptyset$ for $i \neq j$, i.e., there are no subsets that fall into two different classes at the same time. Given an arbitrary pattern x, a classifier aims at associating x with one of the N classes. In this work, we are only concerned in imaging diffractions. Therefore we use two classes ($N = 2$): the diffraction class C_0 and the non-diffraction class C_1 (that includes both noise and reflection image points). We also restrict ourselves to the so-called k-nearest-neighbor (kNN) classifier, because of its simple implementation.

The kNN classifier is a supervised method to solve problems in pattern recognition. It is a method for classifying objects based on a certain distance measure and a fixed set of samples in the feature space for which the associated label of class is already known. The development of the kNN classifier was inspired by the technique for the estimation of a non-parametric probability density function (PDF) called k-nearest-neighbor density estimation, which is basically a variation of the histogram approximation of an unknown PDF. Moreover, although no assumptions about PDFs need to be made, the strategy used by the kNN model to classify patterns reminds of the well-known Bayes classification rule (Duda and Hart, 1973; Theodoridis and Koutroumbas, 1999).

Let $k \leq p$ be a positive fixed integer and $dist$ a distance measure in R^n. Then, the kNN classification process is given by the following rules (Theodoridis and Koutroumbas, 1999)

- Find the k nearest neighbors of x in the set $\{x_1,\cdots,x_p\}$ in terms of their distances $dist(x,x_i)$, for $i = 1,\cdots,p$. Let the symbols $\tilde{x}_1,\cdots,\tilde{x}_k \in \{x_1,\cdots,x_p\}$, with $\tilde{x}_i \neq \tilde{x}_j$ for $i \neq j$, denote those k nearest neighbors.
- Identify the number k_i of patterns $\tilde{x}_i$ among these k nearest neighbors that belong to class w_i for $i = 1,\cdots,N$.
- Assign x to the class w_j with the maximum number k_j of samples.

Figure 2 shows examples of kNN classification for $k = 1$ and $k = 3$.

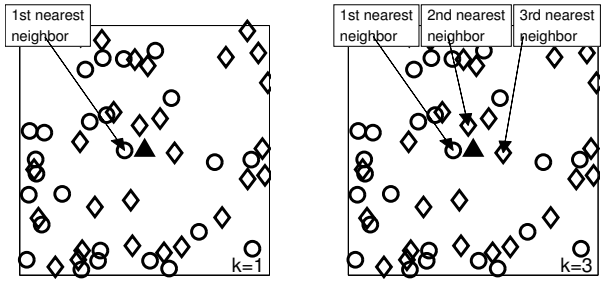

Figure 2: Graphical illustration of kNN classification. (a) For $k = 1$ (one nearest neighbor) the triangle is classified as circle. (b) For $k = 3$ (three nearest neighbors) the triangle is classified as diamond because two of three neighbors are diamonds.

Since the results of a kNN model depend of choice of the number k of nearest neighbors, techniques to select an

appropriate parameter k like, for example, cross-validation, can be employed. Also, the performance may vary as a function of the distance measure considered. Usually, Euclidean distance is used as the distance metric. As with all supervised models, the accuracy of the kNN classifier depends on the given training set. If non-representative samples of classes are used as training data, the performance of kNN classification can be severely degraded.

In the simulations described in the Numerical Examples section, we have employed a value of $k = 1$ and the Euclidean distance measure.

Results and discussion

Synthetic example I: Model with three diffractors

The first model consists of two diffraction points and one dipping reflector with an endpoint in the center of the model, buried in a constant-velocity background with $v = 2000$ m/s (see Figure 3).

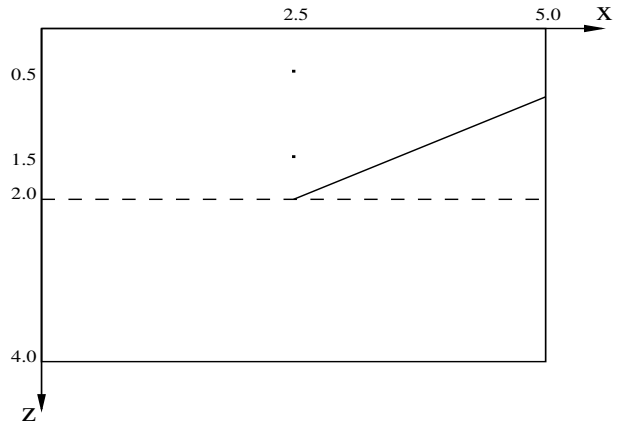

Figure 3: Model with three diffractors.

The synthetic dataset was generated by Kirchhoff modeling. It simulates a zero-offset section with 500 source-receivers pairs spaced at 10 m covering an extension of 5000 m. To the synthetic data we added random noise with a signal-to-noise ratio (S/N) of 100 with respect to the reflection event, which corresponds to a S/N of about 10 for the diffraction events (see Figure 4).

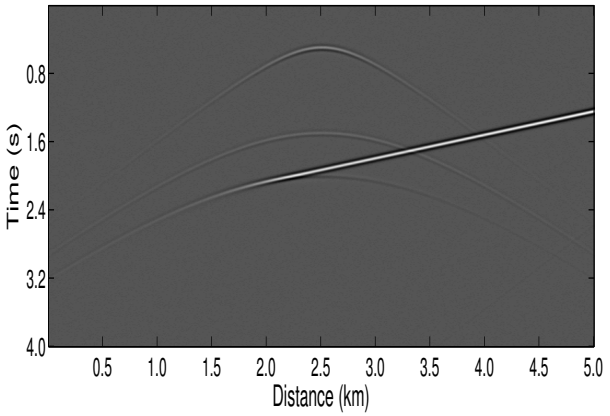

Figure 4: Zero-offset dataset obtained by Kirchhoff modeling.

Conventional Kirchhoff migration of these data produces the image shown in Figure 5. While this image contains all three diffraction points, the two isolated diffraction points have rather low amplitudes and would be hard to visualize in noisy data. Only the endpoint of the reflector is clearly identifiable as a diffraction point. Figure 6 shows the diffraction operators of image locations associated to (a) a void ($x = 2.5$ km, $t = 0.8$ s), (b) a reflection ($x = 3.5$ km, $t = 1.73$ s) and (c) a diffraction ($x = 2.5$ km, $t = 0.5$ s) point, respectively.

As suggested by Landa et.al. (1987), we normalized the dataset trace-by-trace using its envelope (Figure 7). Figure 8 shows the diffraction panels for the profile located at $x = 2.5$ km obtained from the raw data Figure 8a and from the normalized data Figure 8b. The diffraction amplitudes (flat events) are equalized to the reflections (other events). For this case, we started by devising a kNN classifier using only two classes ($N = 2$): the diffraction class C_0 and the non-diffraction class C_1 (that includes both reflection and void image points). To train the kNN classifier, we used the diffraction operators evaluated at the two isolated point diffractors as training patterns for the diffraction class. The training patterns for the non-diffraction class were the diffraction operator at several locations, including reflector and void image points. We then applied the so-trained kNN classifier to the diffraction operators of the whole normalized dataset. The result is depicted in Figure 9.

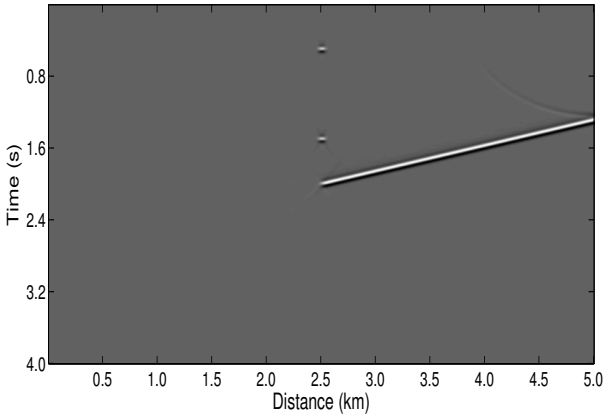

Figure 5: Time-migrated image of dataset from Figure 4.

We see that the method has correctly identified and positioned all three diffractor points in the model, i.e., the two isolated point diffractors used for the training and also the tip of the reflector not used in the training process. Moreover, it has not misidentified any additional points as diffractions.

Synthetic example II: Model with thirteen diffractors

For a more meaningful test, we applied then both methods to a more complex model consisting of 13 diffraction points. There are 4 isolated point scatterers at depths 0.3 km and 0.5 km, 4 tips of reverse faults at 0.7 km and 1.0 km, and 5 tips of normal faults at 2.0 km and 2.3 km depth (see Figure 10). They are buried in a constant-velocity background with $v = 2000$ m/s covering an extension of 8 km in the x direction. The maximum depth of the model is 4 km.

Again, we generated the zero-offset data by Kirchoff

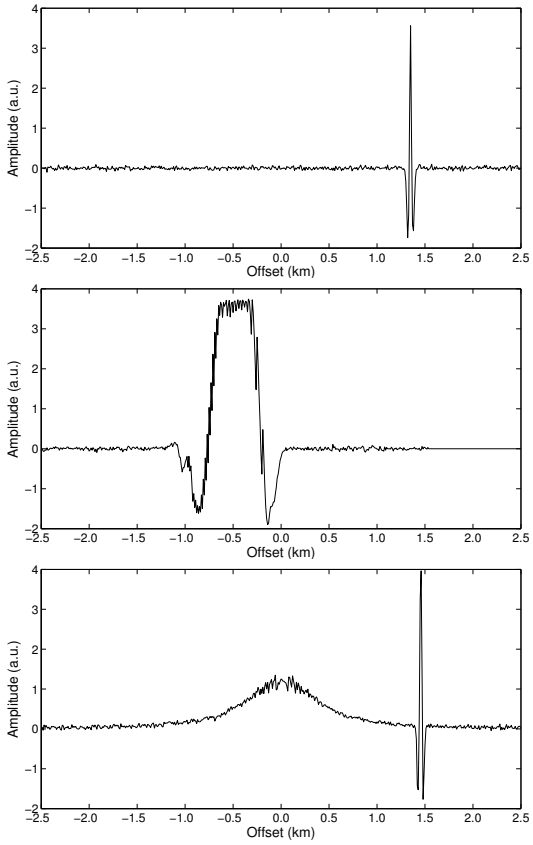

Figure 6: Diffraction operators of image locations in Figure 5 associated to (a) a void ($x = 2.5$ km, $t = 0.8$ s), (b) a reflection ($x = 3.5$ km, $t = 1.73$ s) and (c) a diffraction ($x = 2.5$ km, $t = 0.5$ s) point.

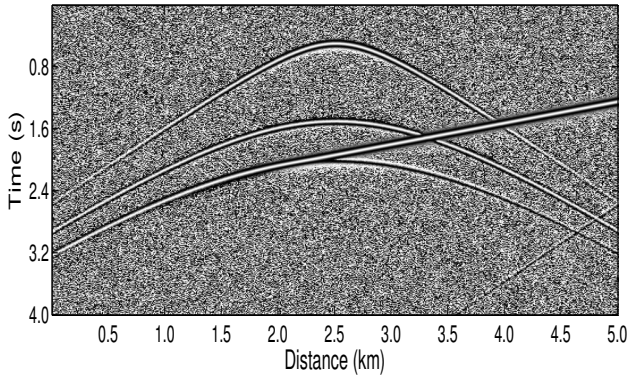

Figure 7: Normalized dataset.

modeling, this time using 800 source-receiver pairs spaced by 10 m with a Ricker wavelet of dominant frequency 12 Hz. Additionally, we added random noise with a signal-to-noise ratio of 100. The generated data and its time-migrated image are depicted in Figures 11 and 12. While the edge diffractors are clearly identifiable in the migrated image in Figure 12, the resolution is insufficient to clearly distinguish the point diffractors at the top of the model. Figure 13 shows the result of the diffraction imaging approach using pattern recognition. For the training of the kNN classifier we used again the points in the first model as described above. From Figure 13, we see that he kNN classifier correctly identified all 13 diffraction points are clearly resolved.

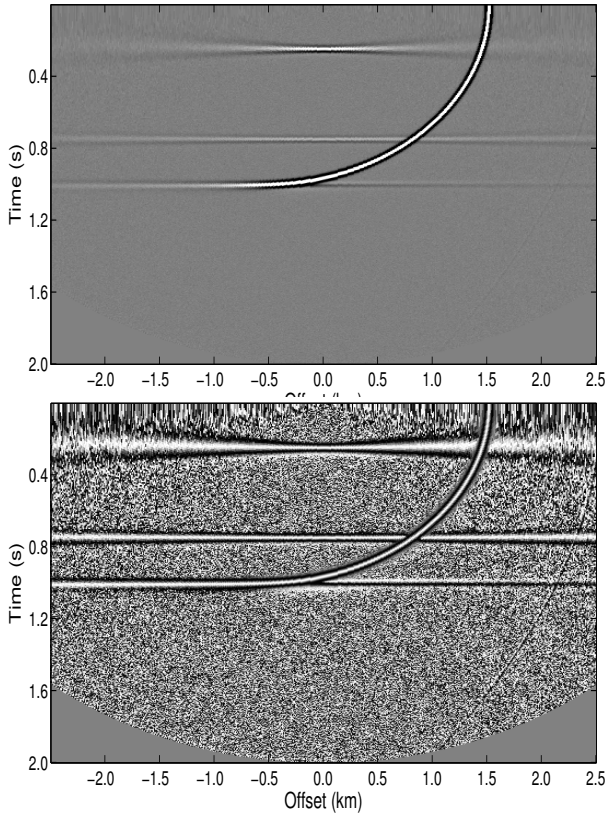

Figure 8: Diffraction panels at 2.5 km obtained from the (a) raw data and (b) normalized data.

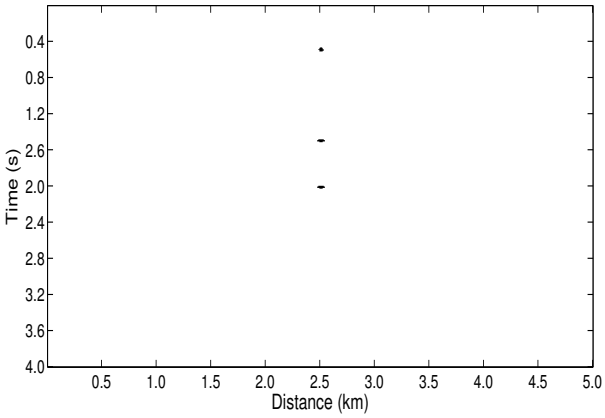

Figure 9: Image points classified as belonging to the diffraction class by the kNN classifier.

It is important to note that the location of the diffractions generated by the normal faults have lower resolution when compared to the others (some smearing can be seen). Other numerical tests (not shown here) indicate that this resolution loss is systematic and can be related to the dip of the faults.

Real data example: Ground Penetrating Radar dataset

For a more meaningful test, we applied this method to GPR data. The data set is from a survey conducted over four metal drain pipes crossing under a road at the University of Houston Coastal Center, located in La Marque, Texas, United States (Figure 14a). Since the survey line was perpendicular to the direction of the pipes, prominent

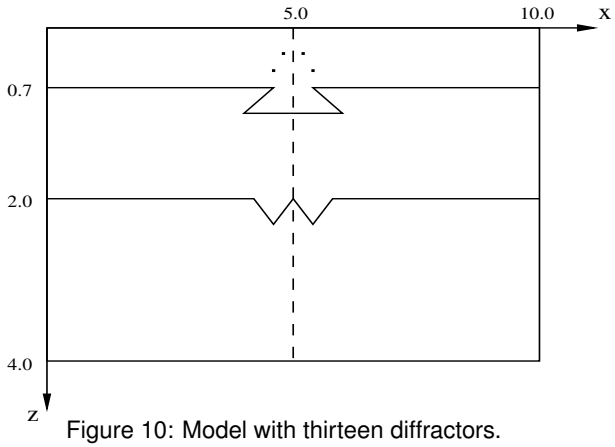

Figure 10: Model with thirteen diffractors.

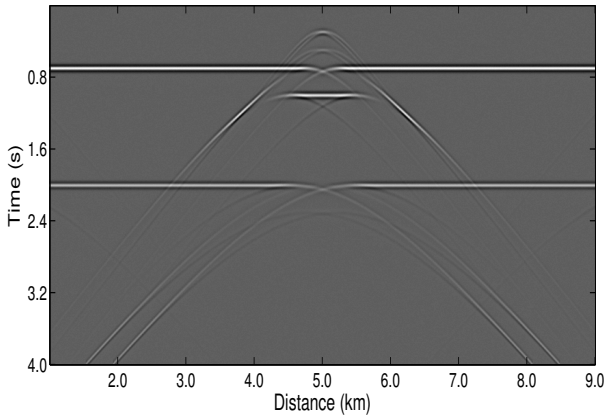

Figure 11: Synthetic zero-offset data for the model of Figure 10.

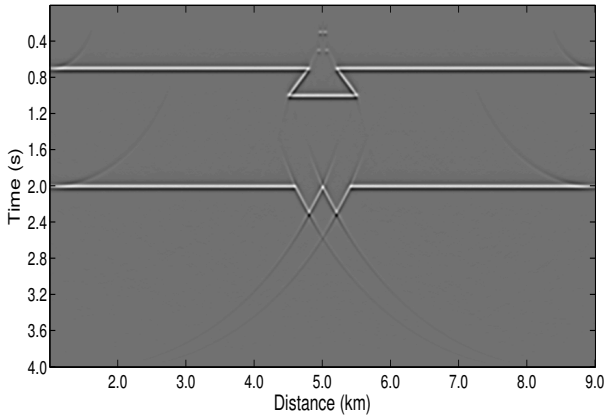

Figure 12: Time-migrated image of the data in Figure 8.

diffractions from the pipes occur. Because of the high reflectivity and attenuation of metal, GPR reflections from the pipes occur only from the exterior of the pipes and not from inside de pipes (Zeng and McMechan, 1997). Figure 14b shows the 250 MHz GPR profile acquired. The distance between the transmitter and reciever antennas was 0.28 m (half-offset 0.14 m), and the interval between traces was 0.05 m. A total of 445 traces were collected along the 22.25 m survey line. The length of the time window was 99 ns and the number of samples per trace was 247, resulting in a time sampling rate of 0.4 ns.

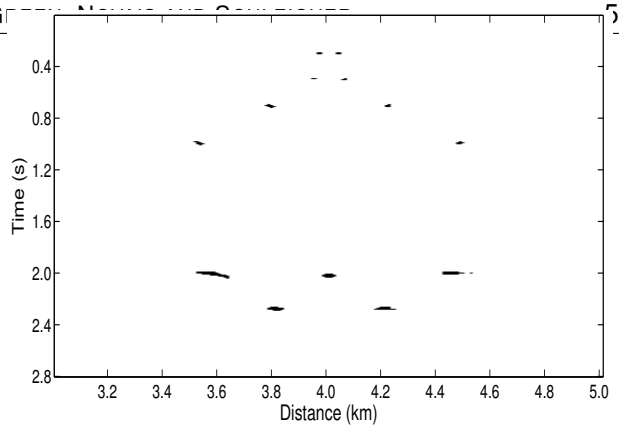

Figure 13: Diffraction locations by kNN classifier. we can see that all 13 diffraction points were indentified.

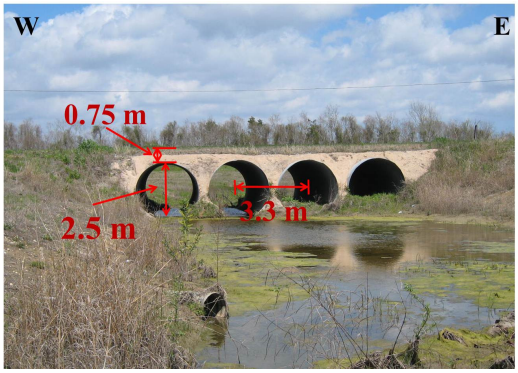

(a)

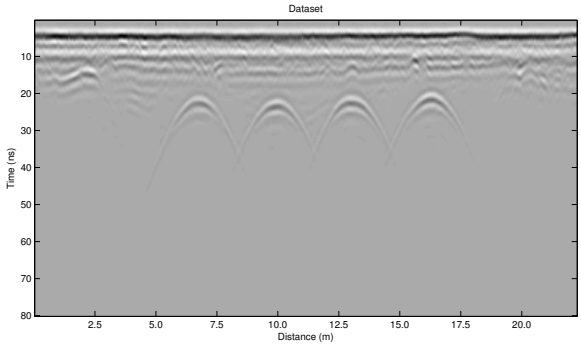

(b)

Figure 14: (a) Metal pipes located in La Marque, Houston, Texas, United States. (b) 250 MHz GPR profile showing diffractions from the pipes.

Figure 15a shows the normalized profile for Figure 14b. Figure 6(b) shows the diffraction panels for the profile located at $x = 10$ m obtained from the normalized data (see Figure 14a). The time migration section using Kirchhoff migration is showing in Figure 15a. The velocity used for migration was 0.088 m/ns (0.88×10^8 m/s). This velocity collapsed diffraction and is within the expected range for soil mixtures. Figure 15b shows the result of the diffraction imaging approach using pattern recognition with the kNN classifier trained on the first synthetic data set.

As we can see from Figure 16b, the application of the so-trained kNN classifier to real GPR field data

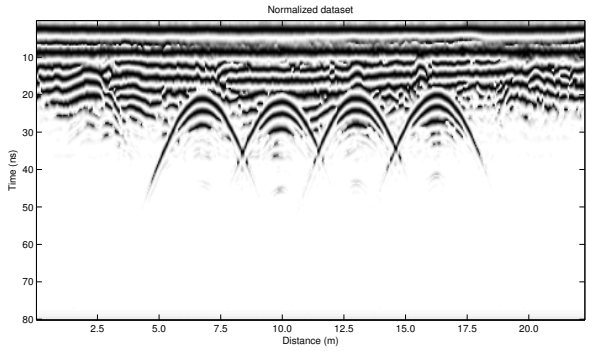

(a)

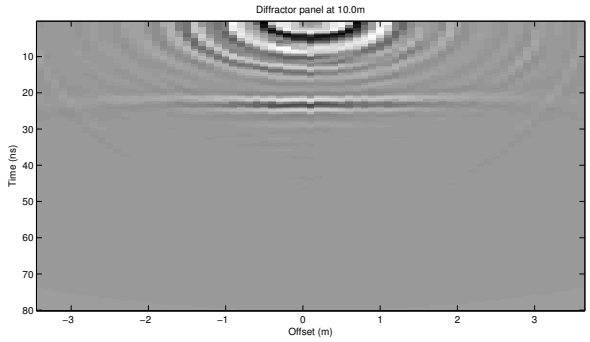

(b)

Figure 15: (a) Normalized GPR data. (b) The diffraction panel for the profile located at $x = 10$ m.

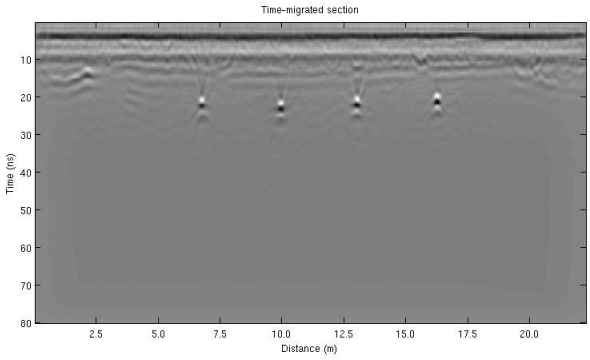

(a)

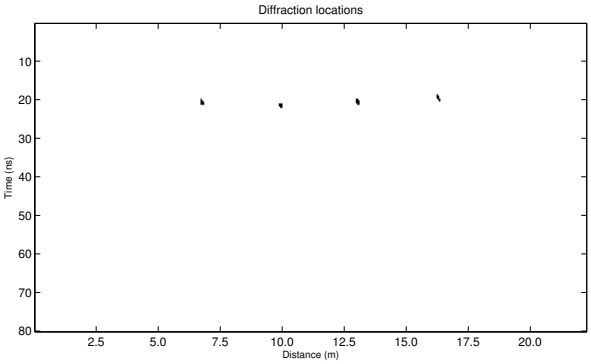

(b)

Figure 16: (a) Time- migration profile. (b) Four diffraction locations identified by kNN classifier.

was successful. Comparing the migrated section (see Figure 16a) with the classified section (see Figure 16b) we can see that the kNN classifier did not produce any false positives and the four diffractions were clearly identified.

Conclusions

In this work, we used the diffractor operator proposed by Tabti et al. (2004) as a tool for diffraction imaging. It consists in a straightforward application of a pattern recognition technique to identify and distinguish diffraction events from reflection events and noise areas by their amplitude pattern. After training with selected diffraction operators pertaining to a synthetic data set from a very simple synthetic model, the kNN classifier was able to correctly detect all diffraction points in a considerably more complicated model and in a real GPR dataset, not missing a single point and not creating a single false positive.

Acknowledgements

The authors wish to thank CAPES, CNPq, and FAPESP, as well as Petrobras and the sponsors of the WIT consortium for financial support. We are grateful to the Allied Geophysical Laboratories team for the GPR data.

References

Duda, R. and Hart, P. , 1973, Pattern Classification and Scene Analysis. *John Wiley & Sons*, New York.

Landa, E. and Keydar, S. , 1998, Seismic monitoring of diffraction images for detection of local heterogeneities. *Geophysics*, 63, 1093 - 1100.

Landa, E., Shtivelman, V., and Gelchinsky, B. , 1987, A method for detection of diffacted waves on commom-offset sections. *Geophysical Prospecting*, 35, 359 - 374.

Moser, T. and Howard, C. , 2008, Diffraction imagining in the depth. *Geophysical Prospecting*, 56, 627 - 641.

Schleicher, J., Hubral, P., Tygel, M., and Jaya, M. S. , 1997, Minimum apertures and Fresnel zones in migration and demigration. *Geophysics*, 62(2), 183 -194.

Schleicher, J., Tygel, M., and Hubral, P. , 1993, 3-D true-amplitude finite-offset migration. *Geophysics*, 58(8),1112 - 1126.

Tabti, H., Gelius, L. J., and Hellmann, T. , 2004, Fresnel aperture prestack depth migration, *First Break*, 22, 39 - 46.

Theodoridis, S. and Koutroumbas, K. [1999] Pattern Recognition, *Academic Press*.

Trorey, A. W. , 1970, A Simple theory for seismic diffractions, *Geophysics*, 35, 762 - 784.

Zeng, X. and McMechan, G. A., 1997, GPR characterization of buried tanks and pipes, *Geophysics*, 62(3), 797 -806.

Zhu, X. and Wu, R.-S., 2010. Imaging diffraction points using the local image matrices generated in prestack migration, *Geophysics*, 75, S1-S9.